

A model-based calibration approach for structural fault diagnosis using piezoelectric impedance measurements and a finite element model

Ahmed Aziz Ezzat¹, Jiong Tang² and Yu Ding³ 

Structural Health Monitoring

1–17

© The Author(s) 2020

Article reuse guidelines:

sagepub.com/journals-permissions

DOI: 10.1177/1475921719901168

journals.sagepub.com/home/shm



Abstract

The electromechanical coupling property of piezoelectric transducers gives rise to a promising class of structural fault diagnosis methods often referred to collectively as impedance-based approaches. One active line of research in the related literature is the development of data-driven methods that can leverage the available experimental impedance measurements to accurately pinpoint the location and severity of structural faults. In this article, we offer a new perspective to the problem by casting the impedance-based fault diagnosis into a statistical calibration formulation, which has gained a wide popularity in the industrial statistics community in the past two decades. Specifically, we decide to estimate the values of the fault attributes (e.g. location and severity) that achieve the closest match between the outputs from a finite element model and those experimentally solicited from the host structure. We further propose to couple this statistical formulation with a pre-screening procedure to reduce the calibration search space and mitigate parameter identifiability issues. In addition to the merit of capably diagnosing structural faults, the proposed approach extends various useful concepts from the statistical calibration literature to the structural health monitoring applications, such as the construction of surrogate models for modeling and predicting impedance changes, the explicit use of a bias function to correct for inherent inadequacies in finite element models, as well as the ability to produce continuous probability distributions for quantifying a fault's severity. These additional benefits substantially enhance both the fault diagnosis capability and computational efficiency. We demonstrate the effectiveness of the proposed approach using two simulated and two experimental case studies from the literature.

Keywords

Calibration, fault detection, fault diagnosis, impedance measurement, piezoelectric, surrogate models

Introduction

A growing trend in the area of structural health monitoring is the use of impedance-based methods for structural fault diagnosis purposes.^{1–7} In theory, the electric impedance signals collected from a piezoelectric transducer are related to the mechanical impedance of the structure to which it is attached. Under harmonic voltage excitation, the piezoelectric impedance measurements are collected from the host structure around a number of structural resonances, resulting in a set of “impedance curves.” These curves can be constantly monitored, and once a departure from a known healthy state is observed, a structural fault is signaled, and then, corrective actions can be recommended. The essence of

impedance-based fault detection methods hinges on this electromechanical correspondence.

An active research challenge in the literature and practice is the development of capable data-driven

¹Department of Industrial & Systems Engineering, Rutgers University, Piscataway, NJ, USA

²Department of Mechanical Engineering, University of Connecticut, Storrs, CT, USA

³Department of Industrial & Systems Engineering, Texas A&M University, College Station, TX, USA

Corresponding author:

Yu Ding, Department of Industrial & Systems Engineering, Texas A&M University, ETB 4016, MS 3131, College Station, TX 77845-3424, USA.
Email: yuding@tamu.edu

procedures that can leverage the available signals from piezoelectric transducers to accurately pinpoint important attributes of structural faults such as the location and severity, among others.² Along that line, statistical indices were proposed in the past to measure the discrepancy between the signals collected before and after damage occurrence and pinpoint the fault attributes.^{8–10} Data mining techniques such as artificial neural networks and support vector machines have also been employed to detect the changes in impedance measurements resulting from structural damages.^{3,11–13} The use of statistical machine learning has also demonstrated its merit in vibration-based structural health monitoring.^{14–18} We note, however, that in certain applications, the high frequency of piezoelectric impedance signals makes them more suitable to detect moderate- and small-sized faults, and hence, the focus of this article is on leveraging the advancements in statistical machine learning to achieve better signal processing and fault diagnosis capability using piezoelectric impedance signals extracted from a target structure.

Model-based approaches, which mostly rely on finite element (FE) models, have recently emerged as powerful tools for impedance-based fault detection purposes. By discretizing the structure into a large number of segments, one would, in theory, be able to match the change in piezoelectric impedance measurements to a change in local mechanical properties and, hence, pinpoint important fault attributes like the severity and location of structural faults through an inverse analysis.^{19–22} A major difficulty standing out in these approaches is the large number of segments often associated with a typical FE discretization, which naturally translates into a large number of unknowns in the inverse analysis. In other words, each segment is treated as a potential fault candidate, and the severity of the potential fault at each segment, often expressed as a percentage change in a local mechanical property, can continuously vary between 0 and 1; all these render the problem often underdetermined, and thus practically difficult to solve.^{20,23,24}

Recent efforts have been devoted toward resolving that issue, among which an approach was proposed which combines a pre-screening procedure, in conjunction with a Bayesian inference analysis, to pinpoint the fault location and severity using impedance measurements and an FE model.²⁴ The pre-screening step is an empirical first-principle-based procedure, employed to reduce the search space into few potential fault locations. Then, the Bayesian sampling scheme, taking advantage of the data, results in more refined posterior estimates of the location and severity of the fault. The idea of combining a pre-screening procedure with a refined data-driven search procedure is indeed promising, but several assumptions can jeopardize the

generalizability of such an approach. Here, we list three crucial assumptions.

First, the method necessitates the discretization of the fault severity variable into a finite number of arbitrary sampling points, so that both the location and severity are treated as discrete variables in the formulation. As such, the quality of the final solution can be dependent on the arbitrary gridding of the severity variable. This also alters the form of the final solution generated from the Bayesian inference, which is a discrete distribution that obviously does not correspond to the continuous nature of the fault severity variable. Second, the Bayesian sampling scheme often requires a considerable number of FE model runs, but doing so is often computationally impractical, especially in impedance-based FE models where the number of segments could be large. Third, the method solely relies on ad hoc pre-tuning and updating techniques to ensure that the FE model used, a critical component in the detection procedure, is well calibrated, so that it can faithfully replicate the behavior of the underlying physical system. It comes as no surprise that the model-based detection approaches are sensitive to any inadequacies in the FE model employed, and when an inadequacy does exist, it is detrimental to the method's detection capability.

To address these challenges, we herein propose a new perspective toward the problem by casting the impedance-based fault detection into a statistical calibration formulation. The method leverages the advancements in statistical learning, together with the power of model-based approaches to achieve accurate fault diagnosis capability. Furthermore, the method can be used in conjunction with the pre-screening step referenced above, which in itself has merit in reducing the search space of possible fault locations, for a computationally practical and effective implementation. But first, let us introduce the background of the statistical calibration and set the stage for how the fault diagnosis problem can be cast into a statistical calibration formulation.

Over the last two decades, statistical calibration has gained a wide popularity in the computer simulation and industrial statistics literature.^{25–28} The use of computer models and simulators to accurately mimic underlying physical processes has been an essential part of designing and operating modern-day engineering systems. An important step in designing these simulators is to calibrate the computer model to be used, to ensure that the computer model in question is an adequate digital representation of the underlying physical system it attempts to mimic. Computer model calibration is formally performed by connecting the outputs from a computer model and those from a physical experiment into one linkage model to simultaneously achieve two

fundamental tasks. The first task is the correction of the inherent bias and inadequacies often found in most computer models, arising due to implicit simplifying assumptions and missing physics. The second task is to estimate a set of unknown parameters, referred to in literature as the “calibration parameters.”²⁵ Calibration parameters are model attributes that cannot be physically observed, controlled, or measured, but whose effect manifests in the response of physical experiments.

In this article, we propose to formulate the structural fault detection problem at hand as a statistical calibration problem. To motivate the essence behind our proposed approach, let us imagine a situation where a piezoelectric transducer is attached to a structure and emits electric impedance measurements. In case of fault occurrence triggered by some change in local mechanical properties, the electric impedance measurements are also expected to exhibit a proportional change, owing to the electromechanical coupling of piezoelectric transducers. Understandably, fault attributes like the location and severity of the fault have a notable effect on the magnitude of that change. Despite their observed effect on the impedance measurements, these fault attributes are not themselves directly observable in the physical experiment, and thus, their values are unknown to the experimenter and have to be inferred.

By establishing the analogy between the setting of a calibration problem, and that of the impedance-based fault detection problem at hand, we can think of the fault attributes such as the location and severity of the fault as calibration parameters, that is, parameters that are not physically observed, yet whose effect is notable on the physical response, and whose presence can be easily included, and values adjusted, in the computer code implementing an FE model. Under that setting, the problem of fault detection is equivalent to that of a calibration problem, where the goal is to estimate the values of the calibration parameters (fault location and severity) that achieve the closest match between the outputs from a computer model (simulated impedance data from the FE model) and those physically collected from the system (piezoelectric impedance measurements), all while accounting for any inherent inadequacies that are associated with the FE model.

The benefits from the proposed approach are multi-fold and do in fact address the three aforementioned limiting assumptions of the existing approach that relies on Bayesian sampling.²⁴ From a broader point of view, we believe that the proposed approach presents a contribution to both the calibration and structural health monitoring fields. From the statistical calibration literature perspective, we have identified a new field of applications for the calibration framework. From the structural health monitoring standpoint, we offer a new perspective toward formulating fault

detection problems under the statistical calibration framework. The proposed method aligns itself with a well-known class of problems known in the structural health monitoring literature as model updating and/or tuning,²⁹ in which an FE model is tuned to faithfully replicate physical experiments and is often cast as a constrained optimization problem^{30,31} or in a Bayesian setting.^{32,33} While having a similar objective, the statistical computer model calibration framework, proposed herein, is methodologically distinct by offering a probabilistic statistical based handling of the problem, which has demonstrated its merit in the industrial statistics literature.^{25,27,34,35} The statistical calibration framework brings in multiple favorable aspects such as the ability to concurrently estimate the calibration parameters and model inadequacy, the use of a surrogate model to replace often computationally expensive FE simulations, its ability to produce probabilistic estimates of the fault severity, as well as on-the-fly probabilistic predictions of the physical output at any combination of inputs. We stress, however, that the statistical calibration framework does not obviate the need for pre-tuning/updating the FE model in the design stage prior to its operational use in fault detection.

The remainder of this article is organized as follows. Section “Statistical calibration of computer models and surrogate modeling” provides a review about the statistical calibration literature and surrogate modeling. Section “Impedance-based fault diagnosis: a statistical calibration approach” discusses the formulation of the fault detection problem under the statistical calibration framework and then proposes a multi-stage algorithm for practical implementation. In section “Case studies,” we demonstrate the effectiveness of our proposed approach on two simulated and two experimental case studies. Finally, we conclude the article in section “Conclusions and future directions” with final remarks and recommendations for future research.

Statistical calibration of computer models and surrogate modeling

High-accuracy computer models capable of accurately replicating and further predicting the behavior of physical processes are essential to a wide variety of real-world applications, stretching from coating processes of food products,²⁶ to nanomanufacturing,^{35,36} to spot welding experiments,³⁴ to reliability assessment of pressurized storage tanks,³⁷ and many others. The role of computer model calibration is to ensure a high-accuracy representation of the physical system by integrating the outputs from the computer model with a set of physical measurements collected from the actual system into a single linkage model.²⁵

Denote by $\mathbf{x} \in \mathbb{R}^d$, the set of controllable inputs in the physical experiment, and by z^p and $z^c \in \mathbb{R}$ as the response from the physical and computer model, respectively, where the superscripts p and c hereinafter denote the physical and computer model, respectively. Oftentimes, the computer model will take the same set of *input variables* \mathbf{x} , in addition to a set of *calibration parameters*, denoted by $\Theta \in \mathbb{R}^k$. These calibration parameters are not observed, controlled, or measured in physical experiments but can be modeled and easily manipulated in the computer model's code. Denote the set of computer model outputs by $\mathbf{Z}^c = [z^c(\mathbf{x}_1, \Theta_1), \dots, z^c(\mathbf{x}_{n^c}, \Theta_{n^c})]^T$, where n^c is the number of computer experiment data. Likewise, one can use $\mathbf{Z}^p = [z^p(\mathbf{x}_1), \dots, z^p(\mathbf{x}_{n^p})]^T$ to denote the set of physical experiment responses, where n^p is the total number of physical measurements.

The goal of the calibration procedure is then to integrate $z^p(\mathbf{x})$ and $z^c(\mathbf{x}, \Theta)$ into one linkage model. One widely accepted formulation for the linkage model, proposed by Kennedy and O'Hagan,²⁵ is expressed in equation (1) below

$$z^p(\mathbf{x}_i) = z^c(\mathbf{x}_i, \Theta) + \gamma(\mathbf{x}_i) + e_i \quad i = 1, \dots, n^p \quad (1)$$

where $\gamma(\cdot)$ is a bias correction term introduced to explicitly correct for any modeling inadequacies in the computer model that arise due to missing physics or inherent simplifying assumptions and e_i is the independent and identically distributed zero-mean normally distributed random variable with its variance denoted by τ^2 .

In many real-world situations, computer models can be computationally expensive to run, and therefore, surrogate models are necessary to construct the response surface of the computer model based on a small number of computer model runs. Among the pool of possible surrogate modeling techniques, Gaussian process (GP) models arise as a nonparametric modeling approach that is widely used as the proxy model for complex unknown functions.³⁸ This is mostly attributed to their interpolative property which is suitable in modeling the response surface of deterministic simulators, as well as their flexibility to model a wide spectrum of response functions, from simple linear patterns to complicated surfaces.³⁹

The pillar assumption in GP models is that the joint distribution of the model output at any finite set of inputs follows a multivariate normal distribution. Under this assumption, a GP model is defined by a mean structure $\mu(\cdot)$ and a stochastic process term $\eta(\cdot)$, as in equation (2)

$$z^c(\mathbf{x}, \Theta) = \mu(\mathbf{x}, \Theta) + \eta(\mathbf{x}, \Theta) \quad (2)$$

where the exact form of $\mu(\cdot)$ is left to be determined by domain knowledge and is designated to capture the global variations in the underlying response function. Oftentimes, $\mu(\cdot)$ is either expressed as a constant, or a linear function of \mathbf{x} and Θ , or some other pre-specified exogenous covariates, such that $\mu(\mathbf{x}, \Theta) = \mathbf{f}^T(\mathbf{x}, \Theta)\boldsymbol{\beta}$, where $\mathbf{f}(\mathbf{x}) = [f_1(\mathbf{x}, \Theta), \dots, f_\ell(\mathbf{x}, \Theta)]^T$ is an $\ell \times 1$ vector of known regression functions and $\boldsymbol{\beta} = [\beta_1, \dots, \beta_\ell]^T$ is the $\ell \times 1$ vector of corresponding unknown regression coefficients. The term $\eta(\mathbf{x}, \Theta)$ is assumed to be a zero-mean GP with its pairwise covariance defined as $\sigma_{ij} = \text{Cov}\{\eta(\mathbf{x}_i, \Theta_i), \eta(\mathbf{x}_j, \Theta_j)\}$. Let us use Σ to denote the resulting $n^c \times n^c$ covariance matrix whose (i, j) th entry is σ_{ij} . Under this setting and for the set of inputs $[(\mathbf{x}_1, \Theta_1), \dots, (\mathbf{x}_{n^c}, \Theta_{n^c})]^T$, the corresponding output is multivariate normal, that is, $\mathbf{Z}^c \sim \mathcal{N}(\mathbf{F}\boldsymbol{\beta}, \Sigma)$, where \mathbf{F} is the $n^c \times \ell$ matrix of covariate values such that its (i, j) th element is $f_j(\mathbf{x}_i, \Theta_i)$, $i = 1, \dots, n^c$, and $j = 1, \dots, \ell$.

A key issue in fitting GPs, however, is to determine the entries of the covariance matrix Σ , which are often dictated through the choice of a suitable stationary parametric covariance function, denoted by $K(\cdot, \cdot; \Phi^c)$, where Φ^c represents a set of covariance parameters, also known as GP hyperparameters. Examples of parametric covariance functions include but are not limited to the squared exponential and the Matérn covariance functions.⁴⁰ Similarly, $\gamma(\cdot)$ in equation (1) can as well be independently modeled as a GP, for which the hyperparameters are denoted by Φ^b .

Given the values for the GP hyperparameters, one can obtain a kriging-based prediction at any unseen test data point $(\tilde{\mathbf{x}}, \tilde{\Theta})$, as expressed in equation (3). Such kriging-based estimate is known to be a best linear unbiased predictor (BLUP)⁴⁰

$$\hat{z}^c(\tilde{\mathbf{x}}, \tilde{\Theta}) = \mathbb{E}\{z^c(\tilde{\mathbf{x}}, \tilde{\Theta}) | \mathbf{Z}^c\} = \mathbf{f}^T(\tilde{\mathbf{x}}, \tilde{\Theta})\boldsymbol{\beta} + \mathbf{k}^T \Sigma^{-1}(\mathbf{Z}^c - \mathbf{F}\boldsymbol{\beta}) \quad (3)$$

where the $n^c \times 1$ vector \mathbf{k} contains the pairwise covariances between \mathbf{Z}^c and $z^c(\tilde{\mathbf{x}}, \tilde{\Theta})$, while \mathbf{Z}^c , $\mathbf{f}(\cdot)$, Σ , \mathbf{F} , and $\boldsymbol{\beta}$ are defined as in equation (2).

With GPs employed to model $z^c(\cdot, \cdot)$ and $\gamma(\cdot)$, the calibration problem reduces to the estimation of the set of calibration parameters Θ , the regression coefficients $\boldsymbol{\beta}$, as well as the GP hyperparameters of the computer model and the bias term, denoted by Φ^c and Φ^b , respectively. Two alternative methods can be used to estimate these sets of parameters. The first method relies on a full Bayesian inference to simultaneously and collectively learn Θ , $\boldsymbol{\beta}$, Φ^c , and Φ^b .²⁵ The other method follows an empirical hierarchical approach and suggests to first estimate $\boldsymbol{\beta}$ and Φ^c using maximum likelihood estimation (MLE) and then plug in the MLE estimates into a Bayesian inference to estimate Θ and Φ^b .³⁴ While the former, in theory, should be more superior, because it

takes into account the uncertainty associated with β and Φ^c , the latter is more computationally efficient, and less prone to implementation breakdowns, while rendering sufficiently close results to the full Bayesian analysis.³⁴ Therefore, we decide to go with the second approach in parameter estimation.

Specifically, we first find the MLEs for Φ^c , which are estimated in a data-driven way by solving the optimization problem in equation (4)

$$\hat{\Phi}^c = \arg \max \left\{ -\ln \left(|\hat{\Sigma}| \right) - \left(\mathbf{Z}^c - \mathbf{F}\hat{\beta} \right)^T \hat{\Sigma}^{-1} \left(\mathbf{Z}^c - \mathbf{F}\hat{\beta} \right) \right\} \quad (4)$$

where $\hat{\Phi}^c$ contains the MLE estimates for Φ^c , $\hat{\Sigma}$ is the covariance matrix, for which the entries are computed using $K(\cdot, \cdot; \hat{\Phi}^c)$, and $\hat{\beta}$ is the generalized least squares (GLS) estimation for β , where $\hat{\beta} = (\mathbf{F}^T \hat{\Sigma}^{-1} \mathbf{F})^{-1} \mathbf{F}^T \hat{\Sigma}^{-1} \mathbf{Z}^c$. The right-hand side in equation (4) is proportional to the logarithm of the likelihood for a GP. The optimization problem in equation (4) is numerically solved using gradient descent-based methods, commonly implemented in practice by calling the MATLAB function `rgp`, or using the routine `nlm` in R. Once these MLEs are obtained, we can plug them into a Bayesian inference scheme to estimate Θ and Φ^b . The Bayesian inference starts by assigning noninformative priors to each parameter and, then, uses a proposal distribution to update the posterior distribution in an Metropolis–Hastings (M–H) Markov chain Monte Carlo (MCMC) algorithm.⁴¹ After a sufficient number of iterations, the M–H algorithm should gradually converge to the underlying posterior distributions of the parameters in Θ and Φ^b . In section “Case studies,” we discuss more details on the implementation of the parameter estimation procedure in the context of the presented case studies.

Impedance-based fault diagnosis: a statistical calibration approach

In this section, we elucidate the foundations of the proposed fault diagnosis formulation following a statistical calibration-based approach. We first explain the key concepts, followed by the formulation of the fault diagnosis problem in a statistical calibration setting. Finally, we propose a multi-stage algorithm for a practical implementation of the proposed methodology.

Modeling of piezoelectric signals

In this work, and without loss of generality, we use the piezoelectric admittance, which is the inverse of the electric impedance, as the response of interest. Physical

piezoelectric admittance measurements can be collected, using a piezoelectric transducer attached to the host structure, at a set of excitation frequencies, denoted by $\omega = \{\omega_1, \omega_2, \dots, \omega_{n^p}\}$. The output from physical experimentation is an “admittance curve,” which shows the admittance values versus the corresponding excitation frequencies. Note that we refer to the excitation frequency variable as ω and the set of excitation frequencies as ω , where the j th element of that set is referred to as ω_j , for $j = 1, \dots, n^p$.

In conjunction with physical experiment data, an FE model is employed to mimic the physical system’s behavior and generate a set of computer experiment data. In a typical FE model, the structure is divided into m segments, where m is often a sufficiently large number. Each segment is further composed of a number of elements, which is the building block of FE models. Under this discretization, an explicit expression of the admittance signal at any given excitation frequency, denoted by $y^c(\omega)$, can be derived,^{21,24,42,43} and is expressed as in equation (5)

$$y^c(\omega) = \frac{\omega i}{q - \mathbf{Q}^T (\mathbf{S} - \omega^2 \mathbf{M} + i\omega \mathbf{B})^{-1} \mathbf{Q}} \quad (5)$$

where i refers to the imaginary unit; q is the inverse of the capacitance of the piezoelectric transducer; \mathbf{Q} is the electromechanical coupling vector; and \mathbf{S} , \mathbf{B} , and \mathbf{M} are the stiffness, damping, and mass matrices, respectively. In this research, we define a fault as a percentage change in stiffness. This definition is physically motivated, since, as shown in equation (5), the piezoelectric admittance is directly dependent on the stiffness matrix \mathbf{S} .

In an FE model, each of the m segments can be subject to fault occurrence. Please note that in this research, we assume that a single fault occurs at a time in the structure. To simulate a fault occurrence in the structure, the FE model takes in a number of inputs: (1) a fault location, expressed as a segment index and denoted by $\theta_1 \in \{1, \dots, m\}$, (2) a fault severity level, expressed as a percentage change in stiffness and denoted by $\theta_2 \in [0, 1]^T$, and (3) a set of excitation frequencies, $\omega = \{\omega_1, \omega_2, \dots, \omega_{n^p}\}$. We assume that the set of excitation frequencies input to the FE model is the same set at which the physical measurements are collected and is as such indexed by n^p . Given these inputs, the FE model outputs a corresponding simulated set of admittance signals. We reflect this input-output dependency through expressing y^c as a function of ω , θ_1 , and θ_2 , therefore denoted by $y^c(\omega, \theta_1, \theta_2)$.

If we set $\theta_1 = \theta_2 = 0$ and run the FE model at the set of excitation frequencies, then no fault is simulated in the structure, and the corresponding set of simulated signals represents the healthy baseline state, denoted by

$y_h^c(\omega, 0, 0)$, where the subscript h implies “healthy.” The difference between the defective and the healthy states is denoted by $\Delta y^c(\omega, \theta_1, \theta_2) = y^c(\omega, \theta_1, \theta_2) - y_h^c(\omega, 0, 0)$ and is used as an indicator of fault occurrence, that is, the response of interest in this research. The vector of impedance change generated at the set of excitation frequencies, $\omega = \{\omega_1, \omega_2, \dots, \omega_{n^p}\}$, is thus referred to as $\Delta y^c(\omega, \theta_1, \theta_2) = [\Delta y^c(\omega_1, \theta_1, \theta_2), \dots, \Delta y^c(\omega_{n^p}, \theta_1, \theta_2)]^T$.

Similarly, we denote by $y^p(\omega) = [y^p(\omega_1), \dots, y^p(\omega_{n^p})]^T$ the set of piezoelectric measurements that are experimentally collected from a piezoelectric sensor attached to the target structure at the set of excitation frequencies ω . Under the baseline healthy state, where no fault is known to exist in the structure, the set of physical measurements are denoted by $y_h^p(\omega)$. For a test structure to be monitored, which can potentially contain a fault, the set of output signals, as mentioned earlier, are denoted by $y^p(\omega)$. The difference between the test and healthy signals is denoted by $\Delta y^p(\omega) = y^p(\omega) - y_h^p(\omega)$ and represents the vector of physical responses to be monitored for fault occurrence, where $\Delta y^p(\omega) = [\Delta y^p(\omega_1), \dots, \Delta y^p(\omega_{n^p})]^T$.

Statistical calibration-based fault diagnosis

Having a set of physical measurements obtained through physical experimentation, and a corresponding set of FE simulation data, one can view the fault location and severity, θ_1 and θ_2 , respectively, as the calibration parameters. Extending on the statistical calibration formulation presented in equation (1), we propose to integrate Δy^p and Δy^c into one linkage model, as presented in equation (6)

$$\Delta y^p(\omega_i) = \Delta y^c(\omega_i, \theta_1, \theta_2; \Phi^c) + \delta(\omega_i; \Phi^b) + e_i \quad i = 1, \dots, n^p \quad (6)$$

By comparing equation (6) with the generic formulation in equation (1), we find that the excitation frequency variable represents the observable input to both the physical and computer experiments, that is, $\mathbf{x} = \{\omega\}$. Furthermore, we find that $z^p = \Delta y^p$, and $z^c = \Delta y^c$, and $\Theta = \{\theta_1, \theta_2\}$, which are the fault location and severity. The goal is to estimate the values of θ_1 and θ_2 which achieve the closest match between the physical and computer model responses.

Impedance-based FE models are often expensive to run due to computational budget limitations. Therefore, we decide to replace the computer model response surface $\Delta y^c(\omega, \theta_1, \theta_2)$ by its surrogate GP model $\Delta \hat{y}^c(\omega, \theta_1, \theta_2; \Phi^c)$, as expressed in equation (7). With the inclusion of a GP surrogate model, it suffices to conduct a few initial simulation runs of the FE model and then construct the underlying response surface of the FE model using a GP model. More

implementation details will be deciphered when presenting the case studies

$$\Delta \hat{y}^p(\omega_i) = \Delta \hat{y}^c(\omega_i, \theta_1, \theta_2; \Phi^c) + \delta(\omega_i; \Phi^b) + e_i \quad i = 1, \dots, n^p \quad (7)$$

We note that the formulation of equation (7) assumes that the change in the experimental signals is explained by a fault occurrence, random noise, or both. This formulation, nevertheless, can be easily extended to account for the impact of other exogenous environmental and operational conditions by regressing the physical response on the exogenous variables of interest or by conditioning the formulation in equation (7) on a set of states within which the operational and/or environmental conditions are homogeneous.⁴⁴ This is beyond the scope of this article but is indeed one potential research extension to this work, which aligns itself well with ongoing research in the structural health monitoring literature.^{44,45}

To summarize, our goal is to pinpoint the true values of the fault attributes, namely, fault location θ_1 and fault severity θ_2 . The true values of these parameters are unknown and, more importantly, not directly observable in a physical experiment, but their physical impact can be observed by an associated signal change. The essence of our procedure is to leverage the statistical calibration framework to find the values of θ_1 and θ_2 that produce the best agreement between the simulation outputs (in which θ_1 and θ_2 can be easily adjusted) and those from the physical experiments (in which θ_1 and θ_2 are not directly observable).

Practical implementation via a multi-stage algorithm

In practice, solving equation (7) is not straight forward owing to the size of the solution space for $\{\theta_1, \theta_2\}$. In impedance-based FE models, m , the number of the candidate fault locations or that of the FE segments, is typically large. On top of that, for each candidate location, the severity level can vary continuously between 0 and 1. Thus, the search space comprising infinite combinations of locations and severities is extremely large. Directly attempting to estimate one single combination of fault location and severity from that large search space is practically cumbersome and can potentially lead to identifiability problems.^{46,47} Here, identifiability refers to the inability to distinguish between the effect of the calibration parameters and that of the computer model bias. Given that our goal is to make a correct inference about the calibration parameters, such issue ought to be properly addressed.

Instead of attempting to directly solve equation (6), we therefore propose an empirical multi-stage procedure that goes around these technical challenges. This

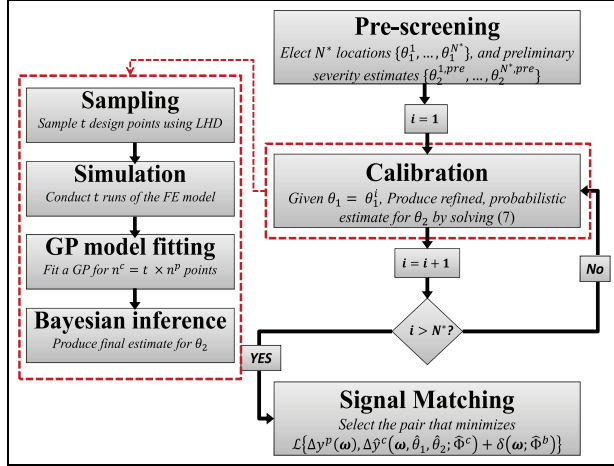


Figure 1. Flowchart of the multi-stage algorithm for impedance-based fault diagnosis.

is to say, we introduce some simple, yet effective, steps to decompose the problem into smaller tractable problems in a knowledge aggregation fashion. Our proposed multi-stage algorithm comprises three stages, where in each stage, we accumulate knowledge by filtering out unlikely location–severity combinations and gradually converge toward the desired solution. The three stages of the proposed algorithm are the following: (1) pre-screening, (2) calibration, and (3) signal matching; see Figure 1 for an illustration. The first stage, that is, pre-screening, aims at reducing the search space into a finite subset of location candidates, with high likelihood of fault occurrence, along with preliminary estimates of their correspondent severity levels. In the second stage, we make use of the pre-screening location/severity estimates to solve a separate calibration problem for each candidate fault location using the pre-screening preliminary estimate as prior information, which results in a refined estimated severity. Then, the goal of the final, third stage is to select the combination of location and severity, of those elected and refined by the first two stages, that minimizes a pre-specified discrepancy measure between the predictions from the final calibrated surrogate model and the observed physical measurements.

We start off by describing the first step. The pre-screening stage is, in fact, the same procedure proposed in a recent fault detection work.²⁴ Our experimental analysis have revealed that this pre-screening procedure is effective in eliminating unlikely location–severity combinations and thus highlighting few potential candidates of high likelihood of fault occurrence, as well as providing preliminary estimates for the severity of these candidates. We here review the key details of this pre-screening step for this article to be self-contained; for more details, please refer to the original paper.²⁴

Let \mathbf{D} be an $m \times 1$ vector defining the fault location and severity as in equation (8)

$$\mathbf{D} = \begin{cases} [0, \dots, 0, \dots, 0]_{m \times 1}^T, & \text{if } \theta_2 = 0 \\ [0, \dots, \theta_2, \dots, 0]_{m \times 1}^T, & \text{if } \theta_2 > 0 \end{cases} \quad (8)$$

such that the vector \mathbf{D} embodies both the fault location and severity information. For instance, if $\theta_1 = 10$ and $\theta_2 = .01$, then the \mathbf{D} vector will contain all zeros except for the 10th element which will have the value of $\theta_2 = .01$.

Based on an inverse sensitivity derivation, the algebraic relationship that relates the physical admittance change vector, $\Delta \mathbf{y}^p(\boldsymbol{\omega})$, and the \mathbf{D} vector can be derived²⁴ and is expressed as in equation (9)

$$\Delta \mathbf{y}^p(\boldsymbol{\omega}) = \mathbf{P} \mathbf{D} \quad (9)$$

where \mathbf{P} is an $n^p \times m$ sensitivity matrix whose entries are computed by the FE model. In theory, an inverse analysis of equation (9) can provide the entries of \mathbf{D} , which embodies the solution to the fault detection problem. Such inverse analysis, as mentioned earlier, is often infeasible due to the underdetermined nature of the problem (due to $m \gg n^p$).

The goal of the pre-screening step is then to overcome that challenge by exploiting the algebraic relationship in equation (9) and computing a directionality index between the columns of \mathbf{P} and $\Delta \mathbf{y}^p(\boldsymbol{\omega})$ for each segment. The motivation behind this directionality index is inspired by the algebraic relation in equation (9), where if a single fault occurs at a specific location, then it is plausible to assume that $\Delta \mathbf{y}^p(\boldsymbol{\omega})$ will be linearly dependent with one of the columns of \mathbf{P} , and thus, the directionality index should be approximately equal to 0, if not exactly so. By ranking these directionality indices, the pre-screening step can elect the N^* top locations, denoted by $\{\theta_1^1, \dots, \theta_1^{N^*}\}$ for further analysis in the second stage. In addition, the pre-screening step computes preliminary estimates of the respective severity levels as

$$\theta_2^{i,pre} = \frac{1}{n} \sum_{j=1}^n \frac{\Delta y^p(w_j)}{p_{ji}}, \quad i = 1, \dots, N^*$$

where p_{ji} is the (j, i) th entry of \mathbf{P} and the superscript *pre* is to stress that these estimates are preliminary estimates, to be differentiated from the refined estimates that will be later obtained in the second stage. In fact, θ_2^{pre} will guide the selection of the Bayesian prior for the calibration analysis in the second stage, thereby ensuring computational efficiency and mitigating the danger of falling to the aforementioned identifiability issues.

The second stage, that is, the statistical calibration, proceeds by solving N^* separate calibration problems

formulated as in equation (7) for each candidate fault location. Unsurprisingly, we start with the most likely candidate fault location as selected by the pre-screening stage and fix the value of $\theta_1 = \theta_1^1$. We then sample t severity levels around $\theta_2^{1,pre}$ using a Latin hypercube design (LHD). The sampled severity levels are denoted by $\{\theta_2^{1,j}\}$, $j = 1, \dots, t$. LHDs are space-filling designs that sample design points in a way to ensure uniform spread over the space of the design variable.³⁹ For each sampled severity level, that is, $j = 1, \dots, t$, we conduct an FE simulation run to generate the simulated admittance change signals at $\theta_1 = \theta_1^1$, $\theta_2 = \theta_2^{1,j}$, and the set of excitation frequencies $\omega = \{\omega_1, \dots, \omega_{n^p}\}$. These simulation runs result in a total of n^c data points, such that $n^c = t$ (design points) \times n^p (excitation frequencies). The simulation model outputs are then subtracted from the healthy state model outputs to obtain a difference vector of n^c data points denoted by $\Delta y^c(\omega, \theta_1, \theta_2)$.

Given the n^c data points, a GP model is then fit to reconstruct the underlying response surface of $\Delta y^c(\omega, \theta_1, \theta_2)$ by solving the optimization problem in equation (4), resulting in an estimated set of GP parameters in $\hat{\Phi}^c$. These parameters, together with a set of priors assigned to θ_2 and Φ^b , are plugged into an M-H random sampling algorithm. For the M-H procedure, the prior for θ_2 will be guided by the pre-screening estimate $\theta_2^{1,pre}$. For instance, a continuous uniform prior can be assigned to θ_2 within a sufficiently broad neighborhood of $\theta_2^{1,pre}$. The Bayesian machinery then gradually updates the prior information in light of the data, until convergence to the final continuous posterior distributions of θ_2 and Φ^b . Statistics like posterior mean, median, and mode can be extracted from the posterior distributions and then used as the point estimates, denoted by $\hat{\theta}_2$ and $\hat{\Phi}^c$, respectively. Specifically, the resulting posterior distribution of θ_2 will represent our data-informed belief about the fault severity at a particular location, and $\hat{\theta}_2$ can be used as our point estimate of the fault severity. This procedure is repeated for all N^* candidates, and the output is N^* pairs of estimated severities and locations, which will be fed to the final stage of the procedure for signal matching and location–severity decision.

The third and final stage is referred to as signal matching, in which, given N^* pairs of location–severity, we select one pair which produces the best agreement between the final calibrated model and the observed physical measurements. This agreement is measured using some pre-specified loss function. Different choices for loss functions can be equally tolerable, but we choose to select the squared error loss measure due to its acceptable usage in the calibration literature.⁴⁷ Similar measures based on the Euclidean distance have also been proposed and widely used in the structural health monitoring literature.⁹ Specifically, the final

signal matching stage finds the pair of location–severity which minimizes the squared error discrepancy among the N^* candidate pairs, as expressed in equation (10)

$$(\theta_1^*, \theta_2^*) = \operatorname{argmin} \sum_{i=1}^{n^p} \left\{ \Delta y^p(\omega_i) - \Delta y^c(\omega_i, \hat{\theta}_1, \hat{\theta}_2; \hat{\Phi}^c) - \delta(\omega_i; \hat{\Phi}^b) \right\}^2 \quad (10)$$

The optimal pair that minimizes equation (10) comprises our final detected fault location and severity estimates.

Case studies

In this section, we demonstrate the effectiveness of our proposed approach on two simulated and two experimental examples taken from the literature.²⁴

Simulated case studies

The first case study simulates a fault occurring in an aluminum cantilevered plate that has been employed extensively in previous investigations,²⁴ with length 0.561 m, width 0.01905 m, thickness 0.004763 m, density 2700 kg/m³, and Young's modulus 68.9 GPa. A piezoelectric transducer is attached at a location that is 0.18 m from the left fixed end. The piezoelectric transducer has length 0.015 m, width 0.01905 m, thickness 0.0014 m, Young's moduli (along two directions) 86 and 73 GPa, density 9500 kg/m³, piezoelectric constant -1.0288×10^9 V/m, and dielectric constant 1.3832×10^8 m/F. This benchmark plate is meshed with 11,250 (375 \times 15 \times 2) 20-node hexahedron elements. The mesh size is smaller than the shortest wavelength of the response involved. The plate is further divided into 225 segments, each containing 50 elements. While self-developed FE code is used in computational analysis to facilitate streamlined process to generate impedance/admittance responses as well as the segmentation procedure, the plate FE model is fully validated using ANSYS with mesh density convergence analysis. Figure 2 shows the dimensions and positions of the plate and transducer, as well as the segmentation of the FE model.

Each segment is a possible fault location, and thus, we have 225 fault location candidates in total. A fault is simulated in the 110th segment with a severity level of .0164, which corresponds to 1.64% change in local stiffness. The piezoelectric impedance measurements are collected around the 14th and 20th structural resonances, which correspond to excitation frequencies of 1893.18 and 3703.09 Hz, respectively. Specifically, 100 frequency values are uniformly sampled around both

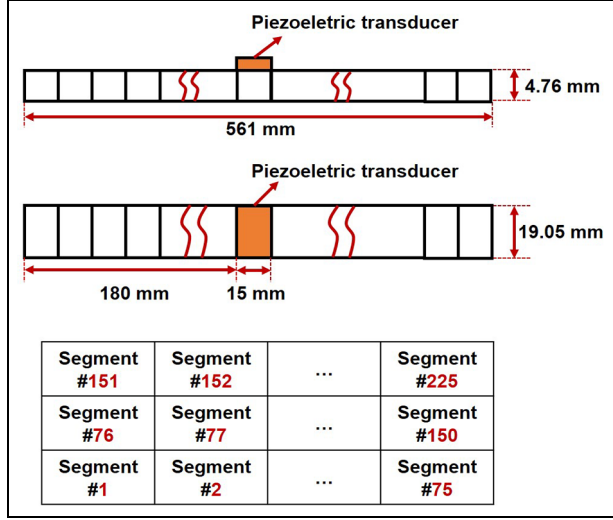


Figure 2. Schematic showing the dimensions and positions of the plate and transducer, as well as the FE segmentation.

1893.18 and 3703.09 Hz, resulting in a total of 200 admittance values at 200 frequencies, that is, $\boldsymbol{\omega} = \{\omega_1, \dots, \omega_{200}\}$. For the final model validation, we reserve a set of the 50 data points to test the predictive ability of the final calibrated model. The 50 data points were randomly selected, such that 25 data points are sampled around the excitation frequency of 1893.18 Hz, and another 25 are sampled around 3703.09 Hz. This leaves $n^p = 150$ data points for implementing the proposed steps of the fault detection procedure as outlined in Figure 1.

A single FE model run is conducted first at $\theta_1 = \theta_2 = 0$ and $\boldsymbol{\omega} = \{\omega_1, \dots, \omega_{150}\}$ to simulate the healthy state signal. Understandably, for simulated examples, this healthy signal represents both the physical system and computer model response at the healthy state such that $y_h^p(\boldsymbol{\omega}) = y_h^c(\boldsymbol{\omega}, 0, 0)$. Then, another FE model run is conducted at $\theta_1 = 110$, $\theta_2 = .0164$, and $\boldsymbol{\omega} = \{\omega_1, \dots, \omega_{150}\}$ to generate the simulated defective signal. Again, because this is a simulated case study, $y^p(\boldsymbol{\omega}) = y^c(\boldsymbol{\omega}, \theta_1 = 110, \theta_2 = .0164)$. The difference vector between the defective and healthy signals is computed as $\Delta y^p(\boldsymbol{\omega}) = y^p(\boldsymbol{\omega}) - y_h^p(\boldsymbol{\omega})$. For this example, $\Delta y^p(\boldsymbol{\omega}) = [\Delta y^p(\omega_1), \dots, \Delta y^p(\omega_{150})]^T$.

The pre-screening stage takes as input $\Delta y^p(\boldsymbol{\omega})$ and \mathbf{P} . Building on the results of a previous study in which the pre-screening procedure was first proposed,²⁴ a ranked list of candidate fault locations is produced, for which we select the top $N^* = 5$ locations for further analysis. The candidate locations that are elected from the pre-screening stage are $\{\theta_1^i\}_{i=1}^{N^*} = \{110, 46, 185, 151, 35\}$, and their respective preliminary estimates of severity are $\{\theta_2^{i,pre}\}_{i=1}^{N^*} = \{.01644, .01350, .01616, .00381, .01734\}$.

Note that the pre-screening step in this example detected the 110th element as one of the selected candidates, which happens to contain the true fault location. Also, in this simulated example, the pre-screening stage was successful in guessing a reasonably accurate estimate for the underlying severity at the 110th element. One might think that it could be enough to stop at this stage since the pre-screening procedure was capable of pinpointing both the location and severity of the fault with reasonable accuracy. We stress, however, that this is mainly because of the nature of the simulated case study which does not involve measurement errors and bias between the physical system and its computer model counterpart. In the experimental case studies, on the other hand, the presence of measurement errors and FE model inadequacies will naturally affect the accuracy of the pre-screening stage and necessitates further, more capable analysis represented in the later stages of our proposed algorithm.

The candidate fault locations and preliminary severity estimates are then fed to the next stage where a calibration problem is solved independently for each location. As explained earlier, we start with the first selected location and fix $\theta_1 = 110$. Then, we generate an LHD of $t = 5$ design points around $\theta_2^{1,pre} = .01644$. The FE model is then run at these 5 design points, resulting in a total of $n^c = t \times n^p = 5 \times 150 = 750$ admittance values. The admittance values are then subtracted from the healthy baseline signals, which results in a 750×1 vector of simulated change signals in $\Delta y^c(\boldsymbol{\omega}, \theta_1, \theta_2)$.

Please note that piezoelectric admittance values, whether physically collected or simulated through the FE model, are complex-valued numbers. To proceed with the calibration framework in equation (7), we then compute the Euclidean norm for the real and imaginary parts. Future research can look into generalizing the approach to complex-valued variables such as piezoelectric admittance. We also standardize the resulting admittance values to facilitate easier GP fitting implementation.

The simulation dataset is then used to fit a zero-mean two-dimensional GP model which reconstructs the underlying response surface of $\Delta y^c(\boldsymbol{\omega}, \theta_1, \theta_2)$. For the GP, we choose the squared exponential covariance function with automatic relevance determination (ARD)⁴⁰ which assigns different length-scale parameters to different input variables and is defined as in equation (11)

$$K((\boldsymbol{\omega}, \theta_2), (\boldsymbol{\omega}', \theta_2')) = \phi_1^c \exp(-r) \quad (11)$$

$$r = \phi_2^c (\boldsymbol{\omega} - \boldsymbol{\omega}')^2 + \phi_3^c (\theta_2 - \theta_2')^2$$

where $\Phi^c = \{\phi_1^c, \phi_2^c, \phi_3^c\} > 0$ are the three parameters representing the sill and the two length scales. An MLE is then implemented to find the parameter values for

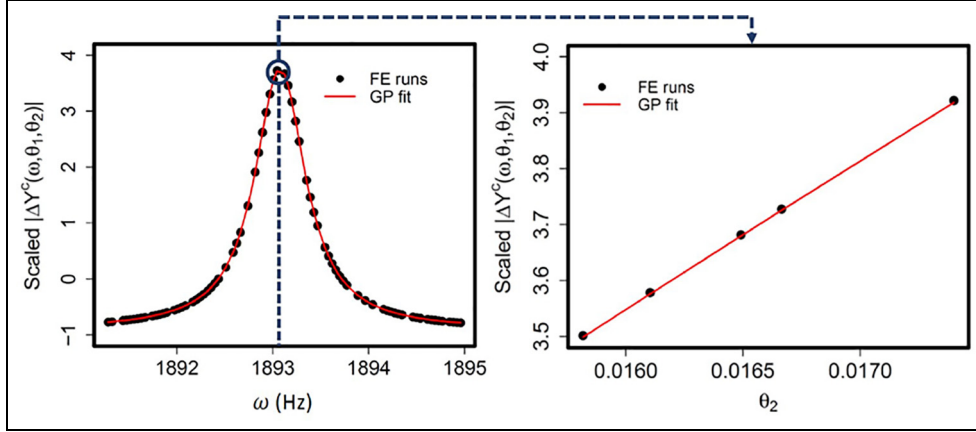


Figure 3. GP fit (red line) versus the FE model runs (black circles) for the first elected fault candidate in the first simulated example. Left panel: GP fit and correspondent FE runs versus excitation frequency ω . Right panel: GP fit and correspondent FE runs versus fault severity θ_2 at $\omega = 1893.18$ Hz. Note how the change in the signal increases, almost linearly, as the fault severity θ_2 becomes more pronounced.

Φ^c that maximize the GP likelihood through a numerical optimization of equation (4). Once MLE estimates are obtained, we now have a surrogate model that represents the underlying response surface of the computer model. This surrogate model can be used to generate a large number of samples, with computation ease, at any given input combination, using the closed form expression in equation (3).

Figure 3 illustrates the GP model fit versus the correspondent FE model runs. On the left panel, the GP output and correspondent FE runs are shown as a function of excitation frequency ω . On the right panel, the GP output and correspondent FE runs are displayed as a function of the fault severity θ_2 at a fixed excitation frequency of $\omega = 1893.18$ Hz. Owing to its interpolative ability, the GP fit passes through every FE run. Notably, the GP fit is able to provide a high-accuracy representation of the FE response surface and can therefore be used as a proxy of the FE model in the statistical calibration analysis. It is worth noting that we only used $t=5$ FE model runs to generate such high-accuracy representation of the model's response surface, which renders a substantial saving in the computational cost when compared to fault detection methods that require FE model runs at each step of the search procedure.

The MLE estimates are then plugged into the M-H algorithm that finds the posterior distributions of θ_2 and Φ^b . For the bias term, we use a zero-mean one-dimensional GP with a squared exponential covariance function. Thus, the GP for the bias term is only characterized by two parameters corresponding to the sill and length-scale parameters, respectively, that is, $\Phi^b = \{\phi_1^b, \phi_2^b\}$.

For the M-H algorithm, we assign the following Bayesian priors to θ_2 , ϕ_1^b , and ϕ_2^b , respectively, as in equation (12)

$$\begin{aligned} p(\theta_2) &= \text{Unif}(.01544, .01744) \\ p\left(\frac{1}{\phi_1^b}\right) &= \text{Gamma}(1, 10^{-3}) \\ p(\exp(-\phi_2^b)) &= \text{Beta}\left(1, \frac{1}{2}\right) \end{aligned} \quad (12)$$

where $p(\cdot)$ denotes a prior distribution, $\text{Unif}(\cdot, \cdot)$, $\text{Beta}(\cdot, \cdot)$, and $\text{Gamma}(\cdot, \cdot)$ denote the continuous uniform, beta, and gamma distributions, respectively. The motivation behind the selection of the priors is as follows. For the fault severity θ_2 , we would like to reflect our weak belief in the pre-screening estimate. For that, we use the continuous uniform distribution but set the uniform distribution parameters to be within a symmetric broad enough interval around the pre-screening estimate. A gamma distribution is selected for the precision (the inverse of the sill in the squared exponential covariance function) which is a common choice in the case of a zero-mean GP, while a beta distribution is selected for the exponential of the length-scale parameter ϕ_2^b as it has shown to ensure numerical stability and positivity in our estimation procedure. In general, the M-H algorithm is agnostic to the choice of priors as long as a "proposal distribution" is adequately selected (in our context, we choose a normal distribution) to construct a Markov chain for which the long-run distribution approximates the posterior distribution. Moreover, there is numerical evidence in the literature that the choice of priors for a squared exponential covariance function has little

Table 1. Final statistics for posterior distributions of severity estimates.

θ_1	Mean (θ_2)	Median (θ_2)	Mode (θ_2)	Standard deviation
110	.01639	.01639	.01652	9.74×10^{-5}
46	.01314	.01316	.01308	2.50×10^{-4}
185	.01613	.01614	.01621	3.93×10^{-4}
151	.00390	.00391	.00391	2.60×10^{-5}
35	.01711	.01695	.01642	6.20×10^{-4}

Bold-faced values indicate median point estimates.

Table 2. Final signal matching values.

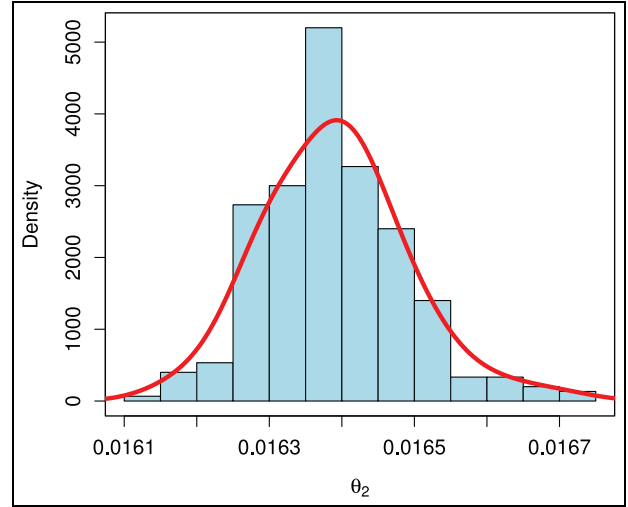
(θ_1, θ_2)	SSE
(110, .01639)	4.82×10^{-5}
(46, .01316)	5.10×10^{-5}
(185, .01614)	4.92×10^{-5}
(151, .00391)	7.11×10^{-5}
(35, .01694)	6.08×10^{-5}

SSE: sum of squared errors.

The value in bold is the smallest.

impact on hyperparameter estimation and predictability of a GP model.⁴⁸ The M-H algorithm is run for 3000 MCMC iterations, thinned every 10 observations to reduce the between-sample autocorrelations. The above procedure is repeated for all N^* locations, and the final posterior statistics for the posterior distributions of the severity estimates are shown in Table 1. In this research, we use the posterior medians as the point estimates for the severity level, indicated as bold-faced values in Table 1.

We then proceed to the final step of our proposed multi-stage procedure. For each candidate fault location, we use the final calibrated surrogate model to issue predictions for the observed physical data points. The predictions from the N^* pairs of location–severity are compared using the sum of squared errors (SSE) loss to measure the discrepancy between the physical outputs from the underlying system and those obtained using the final calibrated surrogate models. The output from this comparison is presented in Table 2. The pair of location–severity which achieves the minimum discrepancy in the signal matching step represents our final detected pair, which in this case is $(\theta_1^*, \theta_2^*) = (110, .01639)$. Unsurprisingly, the true fault occurs at the 110th element and at a severity level of .01640, substantially close to the estimates from our procedure. In Figure 4, the final posterior distribution of the severity estimate is shown, which shows a peak almost around the true severity level.

**Figure 4.** Posterior distribution for the estimated severity level for the first simulated example.

As mentioned earlier, the benefits reaped from the proposed calibration-based approach are multifold. First, we were able to produce continuous probabilistic estimates for the severity level as illustrated in Figure 4. In other words, we avoided the need for arbitrary discretization of the severity level variable, a common undertaking in previous research studies. Second, the final outcome of the approach is a calibrated surrogate model that closely replicates the output from the physical system. More than that, the model is also able to produce predictions of the signal change at unseen excitation frequencies. In Figure 5, we plot the actual (scaled) physical data (black circles) around the 1893.18 Hz, along with the model fit of the calibrated model (dashed blue line). We also plot the reserved test data points (red triangles), along with the final model predictions (green crosses) for these test points. Note how the model fit from the calibrated model is able to replicate the behavior of the underlying physical system, all while producing accurate predictions for unseen test points.

For the second simulated example, the true fault location is set at the 115th segment, and the true severity level is set at .02167. The pre-screening step elects 5 candidate locations: $\{\theta_1^i\}_{i=1}^{N^*} = \{148, 139, 223, 73, 115\}$, along with their respective preliminary estimates: $\{\theta_2^{i,pre}\}_{i=1}^{N^*} = \{.06589, .03050, .06446, .06351, .02144\}$. Again, the pre-screening step was able to include the true fault location among the top 5 candidates, although not necessarily ranked first, which confirms the need for more in-depth analysis in the second and third steps.

Similar to the first simulated example, a separate calibration problem is solved for each location

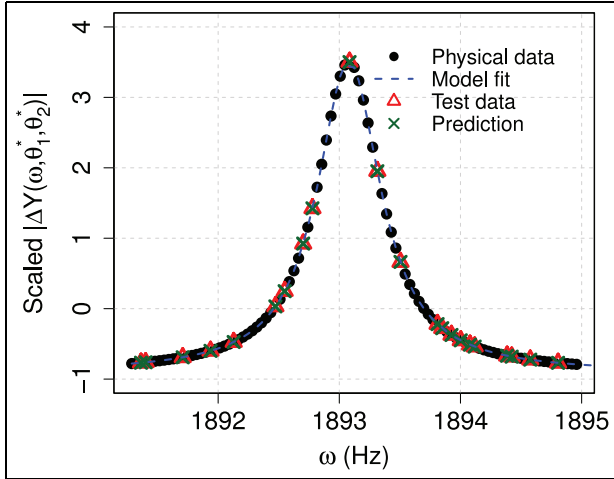


Figure 5. Calibrated model fit (dashed blue line), physical data (black circles), test data (red triangles), and the model predictions (green crosses) for the first simulated example.

Table 3. Final statistics for posterior distributions of severity estimates for the second simulated example.

θ_1	Mean (θ_2)	Median (θ_2)	Mode (θ_2)	Standard deviation
148	.06592	.06593	.06491	5.72×10^{-4}
139	.03055	.03057	.03084	5.24×10^{-4}
223	.06441	.06447	.06446	5.84×10^{-4}
73	.06321	.06354	.06351	5.77×10^{-4}
115	.02152	.02157	.02139	5.21×10^{-4}

Bold-faced values indicate median estimates.

candidate using $t=5$ design points, randomly sampled again via an LHD. The posterior statistics of the severity estimates for each location are shown in Table 3. The signal matching step is conducted, and the squared error discrepancy values are presented in Table 4. Here, the last pair, $(\theta_1^*, \theta_2^*) = (115, .02157)$, presents the closest match between the physical outputs and those from the calibrated surrogate model. Note that the calibration analysis was able to refine the severity level at the 115th segment from its pre-screening estimate at $\theta_2^{5,pre} = .02144$ to a more refined posterior estimate of $\theta_2^* = .02157$. Figure 6 shows the posterior distribution of the estimated severity level at the 115th segment. Figure 7 shows the calibrated model fit to the available physical data points, as well as its predictions to the unseen test points.

Experimental case studies

We now proceed to the experimental case studies using actual physically collected piezoelectric measurements.

Table 4. Final signal matching values for the second simulated example.

(θ_1, θ_2)	SSE
(148, .0659)	8.10×10^{-11}
(139, .0306)	5.04×10^{-8}
(223, .06445)	1.05×10^{-10}
(73, .0635)	1.85×10^{-10}
(115, .02157)	5.21×10^{-12}

SSE: sum of squared errors.

The value in bold is the smallest.

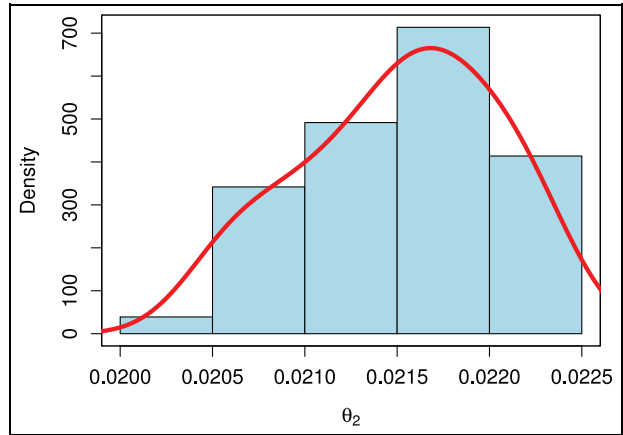


Figure 6. Posterior distribution for the estimated severity level for the second simulated example.

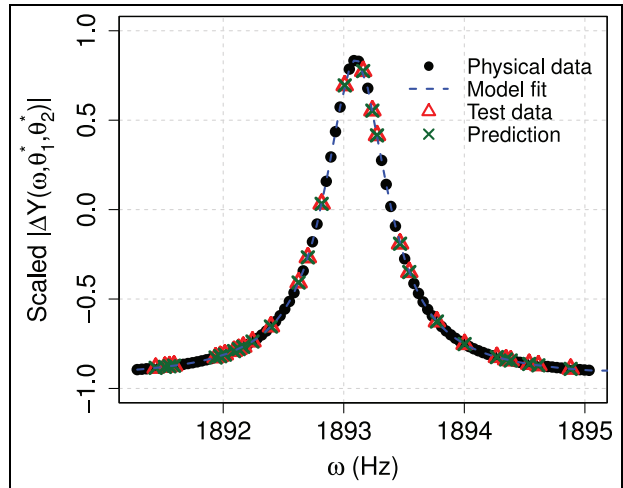


Figure 7. Calibrated model fit (dashed blue line), physical data (black circles), test data (red triangles), and the model predictions (green crosses) for the second simulated example.

The experimental setup is the same as the simulation case studies' setup (shown in Figure 2). One advantage of piezoelectric impedance/admittance technique is that

the data acquisition is easy to realize. A signal analyzer (Agilent 35670A) with a source channel is employed to generate sinusoidal voltage sent to piezoelectric transducer V_{in} . To obtain the piezoelectric admittance, a resistor of $R_s = 100\Omega$ is connected in series with the piezoelectric transducer to measure the voltage drop V_{out} , which yields the admittance information as $\frac{V_{out}}{R_s V_{in}}$. Frequency sweeping excitations are applied, and then, the admittance values are measured under a series of excitation frequency points. In addition, a pre-tuning/ updating procedure is employed prior to the operational use of the FE model in fault detection where healthy signals were used to tune the output of the FE model by solving a numerical optimization procedure in which the stiffness values at the fixed edge were determined to minimize the deviation between the model and physical responses. For the first experimental case study, a mass of 0.6 g is attached to the structure at a location corresponding to the 110th segment in the FE model, which approximately reproduces the effect of a 1.6% change in local stiffness due to a local fault. A total of 200 admittance measurements are physically collected from the structure, before and after the fault, around the excitation frequencies of 1893.18 and 3703.09 Hz.

Similar to what was done in the simulation case studies, we reserve 50 data points for evaluating the final model predictive power. The change in admittance signals is calculated as the difference between the defective and healthy admittance vectors and used as input to the pre-screening stage, which elects the $N^* = 5$ candidate locations as the following: $\{\theta_1^i\}_{i=1}^{N^*} = \{110, 35, 46, 185, 151\}$, along with their correspondent preliminary severity estimates: $\{\theta_2^{i,pre}\}_{i=1}^{N^*} = \{.01590, .01635, .01286, .01534, .00363\}$.

For each location candidate, we generate an LHD of $t=5$ samples around the pre-screening severity estimate. The FE model is run at these 5 design points, leading to $5 \times 150 = 750$ data points. A single FE run is conducted with $\theta_1 = \theta_2 = 0$ to obtain the model output under the healthy condition. The change in admittance is then computed as the difference between the defective and healthy FE model output vectors. Using these 750 data points, a GP model is fit and used as the computationally cheap high-accuracy proxy for the FE model response surface. In all experimental examples, the noise variance is set at $\tau^2 = 10^{-6}$. We run the M-H algorithm for 4000 iterations, thinned every 10th sample. The final posterior statistics for the posterior distributions of the severity level are presented in Table 5. The discrepancy between the physically collected values and the predictions from the model is measured using the SE loss, as presented in Table 6. The final pair with the minimal squared error discrepancy is $(\theta_1^*, \theta_2^*) = (110, .01584)$, while the true location of the

Table 5. Final statistics for posterior distributions of severity estimates for the first real-world example.

θ_1	Mean (θ_2)	Median (θ_2)	Mode (θ_2)	Std-dev
110	.01582	.01584	.01590	1.21×10^{-4}
35	.01620	.01622	.01635	1.13×10^{-4}
46	.01230	.01221	.01286	2.92×10^{-4}
185	.01479	.01483	.01534	3.09×10^{-4}
151	.00309	.00304	.00363	3.36×10^{-4}

Bold-faced values indicate median estimates.

Table 6. Final signal matching values for the first real-world example.

(θ_1, θ_2)	SSE
(110, .01584)	.00098
(35, .01622)	.00127
(46, .01221)	.00113
(185, .01483)	.00101
(151, .00304)	.02615

SSE: sum of squared errors.

The value in bold is the smallest.

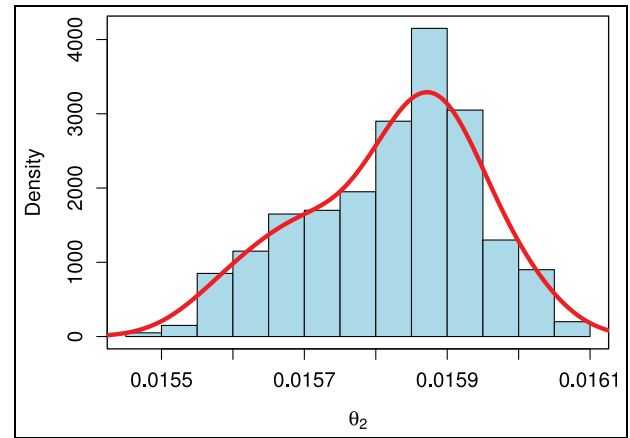


Figure 8. Posterior distribution for the estimated severity level for the first real-world example.

fault is indeed at the 110th segment, with a severity of .0160. Again, the proposed approach is able to accurately pinpoint the location and severity level of the fault. Figure 8 illustrates the posterior distribution of θ_2 .

We test the predictive ability of the final calibrated model on the unseen test data. Figure 9 shows the actual data (black circles), along with the surrogate model fit (dashed blue line) and its predictions (green crosses) to the test points (red triangles). Different from the earlier plots, we plot in Figure 9 the predictions from the uncalibrated surrogate model which was

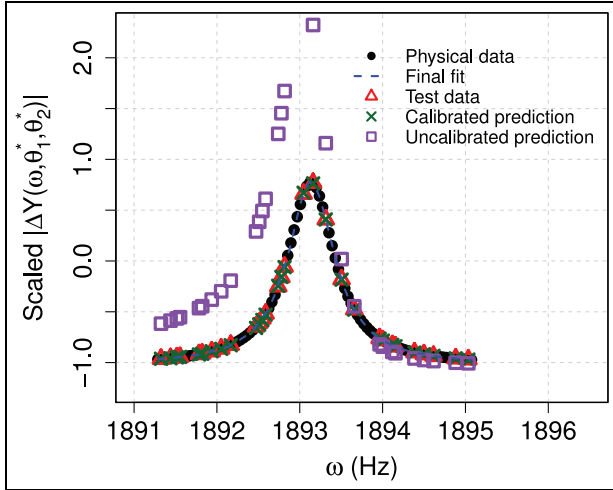


Figure 9. Calibrated model fit (dashed blue line), physical data (black circles), test data (red triangles), the final calibrated surrogate model predictions (green crosses), as well as the uncalibrated surrogate model predictions (purple squares) for the first real-world example.

Table 7. Final statistics for posterior distributions of severity estimates for the second real-world example.

θ_1	Mean (θ_2)	Median (θ_2)	Mode (θ_2)	Standard deviation
139	.03504	.03505	.03531	1.76×10^{-4}
224	.31307	.31308	.31358	2.01×10^{-4}
74	.31024	.31025	.31076	2.19×10^{-4}
149	.32932	.32935	.32966	2.21×10^{-4}
115	.02506	.02506	.02532	1.58×10^{-4}

constructed solely using the FE runs (purple squares). It is obvious from Figure 9 that the uncalibrated response surface exhibits a noticeable bias resulting from overestimating the change signal in some regions of the frequency domain. Through the explicit modeling of the bias term, $\delta(\omega)$, our proposed procedure is able to account for such model inadequacies, yielding the final calibrated surrogate model fit (dashed blue line).

For the second experimental example, the fault is located at the 115th segment, with a severity level of .0250. The physical admittance measurements are collected before and after the fault, and the pre-screening stage yields the following candidate locations: $\{\theta_1^i\}_{i=1}^{N^*} = \{139, 224, 74, 149, 115\}$, along with their correspondent preliminary estimates for the severity levels: $\{\theta_2^{i,pre}\}_{i=1}^{N^*} = \{.03436, .31259, .30981, .32868, .02437\}$. After the second and third stages, the posterior statistics for the severity level at each candidate location are shown in Table 7 and the discrepancy values are shown in Table 8.

Table 8. Final signal matching values for the second real-world example.

(θ_1, θ_2)	SSE
(139, .035)	7.42×10^{-7}
(224, .313)	9.70×10^{-7}
(74, .310)	8.91×10^{-7}
(149, .329)	9.46×10^{-7}
(115, .0251)	6.44×10^{-7}

SSE: sum of squared errors.

The value in bold is the smallest.

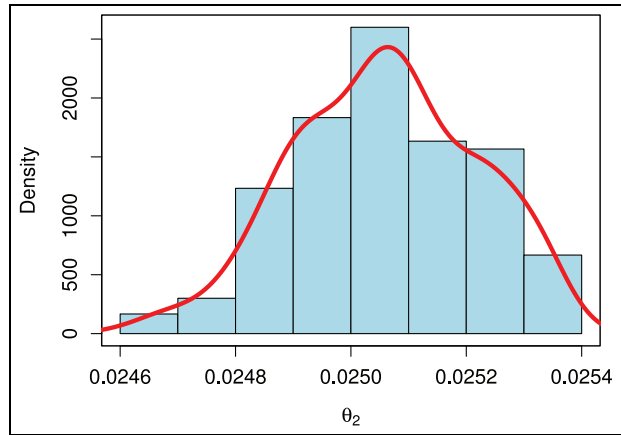


Figure 10. Posterior distribution for the estimated severity level for the second real-world example.

The detected fault location and severity with the minimal squared error discrepancy is $(\theta_1^*, \theta_2^*) = (115, .02506)$ which is rather close to the actual fault location at the 115th segment and its correspondent true severity at .0250. Figure 10 shows the posterior distribution of the detected severity level. The final calibrated model fit is illustrated in Figure 11 (the blue dashed line). Again, the response from the uncalibrated surrogate model is plotted to make it easier to appreciate the benefit from the computer model calibration.

In summary, as demonstrated by the simulated and experimental case studies, our proposed calibration-based procedure is able to successfully pinpoint the location of the fault in all experiments, as well as provide probabilistic estimates of the fault severity with a satisfactory degree of accuracy. While an empirical data-driven approach like the pre-screening method has value in providing preliminary estimates, it cannot, by itself, provide a robust detection performance, not to mention its inability to produce probabilistic estimates for the fault severity, and forward-looking predictions of the resulting signal change. Table 9 provides

Table 9. Statistical performance of the calibration-based (CL) method versus the pre-screening (PS) method as a benchmark.

	$\mathbb{I}(\theta_1^* = \theta_1)$		$ \theta_2^* - \theta_2 $	
	CL	PS	CL	PS
Case #1	1.00	1.00	1.00×10^{-5}	4.00×10^{-5}
Case #2	1.00	0.00	1.00×10^{-4}	4.42×10^{-2}
Case #3	1.00	1.00	1.60×10^{-4}	1.00×10^{-4}
Case #4	1.00	0.00	1.00×10^{-4}	1.01×10^{-2}

CL: calibration-based; PS: pre-screening.

The first two columns show the detection accuracy of the fault location θ_1 , where $\mathbb{I}(\cdot)$ is an indicator function returning 1 if the true location of the fault is detected. The third and fourth columns show the absolute deviation between the estimated and true fault severity levels (lower the better).

Except for the third case study where the detection performance of both CL and PS are comparable, the CL approach provides superior, and more importantly, robust performance in detecting the fault location and severity attributes.

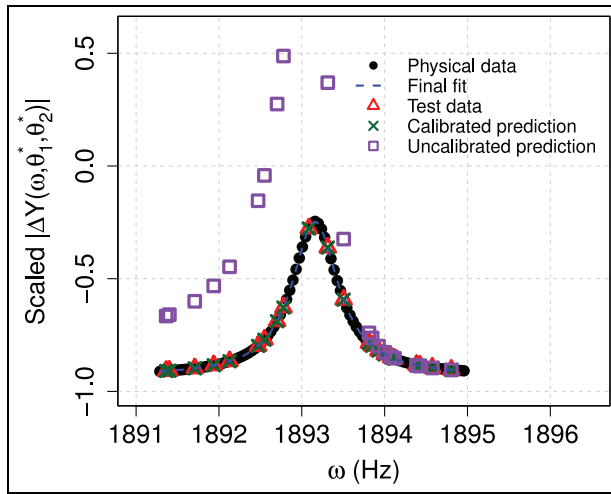


Figure 11. Calibrated model fit (dashed blue line), physical data (black circles), test data (red triangles), the surrogate model predictions (green crosses), and the uncalibrated model predictions (purple squares) for the second real-world example.

statistical estimates on the performance of our proposed calibration-based approach relative to the pre-screening method as a benchmark.

Conclusions and future directions

In this article, we present a new formulation for impedance-based structural fault detection by casting the fault detection problem into a computer model calibration framework. Toward enabling a feasible and practical solution, we propose a multi-stage algorithm, which starts with a first principle-based pre-screening step for reducing the search space by electing a few, but likely, candidate locations, along with the preliminary estimates for the correspondent severity levels. A calibration problem is then solved independently for each respective candidate location, providing refined

combinations of location–severity. The final detected fault location and severity is then decided through a signal matching step which measures the discrepancy between the signals collected from the underlying physical system and those predicted by the final calibrated surrogate model.


Using two simulated and two experimental case studies from literature, we have demonstrated the merit of our proposed approach in terms of its detection capability and reduced computational demands. The adoption of the calibration approach brings in multiple useful features: the use of surrogate models for substantial computational savings, the explicit modeling of bias correction functions, and the generation of continuous probabilistic estimates for the fault severity. We hope that the demonstrated promise of the calibration-based approach would be a solid step toward more elaborate studies that leverage the statistical calibration framework in structural health monitoring applications beyond our proposed multi-stage algorithm.

One opportunity for improving our proposed method is to devise a systematic procedure to automatically tune some of the method's inputs such as the choice of the N^* pre-screening locations (in stage 1) and the number of design samples around each pre-screening location (in stage 2), as dictated by the risk utility of the user and the application under consideration. One of our future research directions is to provide a more general solution approach that may tackle the formulation in equation (7) directly and hence would naturally require less user-based decisions. Additional interesting research extensions of this work are to consider and distinguish the effect of environmental and operational conditions on the physical signals apart from the damage effects, which has been a matter of active research in the structural health monitoring literature. Finally, the handling of complex-valued variables in GP modeling is also a worthy topic, solution to which may find broader set of applications beyond structural health monitoring.

Funding

The author(s) disclosed receipt of the following financial support for the research, authorship, and/or publication of this article: J.T. was supported in part by NSF under Grant No. CMMI-1544707. A.A.E. and Y.D. were supported in part by NSF under Grant No. CMMI-1545038.

ORCID iD

Yu Ding  <https://orcid.org/0000-0001-6936-074X>

References

1. Annamdas VGM and Radhika MA. Electromechanical impedance of piezoelectric transducers for monitoring metallic and non-metallic structures: a review of wired, wireless and energy-harvesting methods. *J Intel Mater Syst Struct* 2013; 24(9): 1021–1042.
2. Annamdas VGM and Soh CK. Application of electromechanical impedance technique for engineering structures: review and future issues. *J Intel Mater Syst Struct* 2010; 21(1): 41–59.
3. Giurgiutiu V and Zagrai A. Damage detection in thin plates and aerospace structures with the electro-mechanical impedance method. *Struct Health Monit* 2005; 4(2): 99–118.
4. Gresil M, Yu L, Giurgiutiu V, et al. Predictive modeling of electromechanical impedance spectroscopy for composite materials. *Struct Health Monit* 2012; 11(6): 671–683.
5. Min J, Park S, Yun CB, et al. Impedance-based structural health monitoring incorporating neural network technique for identification of damage type and severity. *Eng Struct* 2012; 39: 210–220.
6. Park S, Yun CB and Inman DJ. Structural health monitoring using electro-mechanical impedance sensors. *Fatigue Fract Eng M* 2008; 31: 714–724.
7. Zhou W and Zuo L. Sensitivity-enhanced admittance-based structure health monitoring using a higher-order resonant circuit. *Smart Mater Struct* 2012; 21(10): 105023.
8. de Souza Rabelo D, Valder Steffen J, Neto RMF, et al. Impedance-based structural health monitoring and statistical method for threshold-level determination applied to 2024-t3 aluminum panels under varying temperature. *Struct Health Monit* 2017; 16(4): 365–381.
9. Giurgiutiu V and Rogers CA. Recent advancements in the electromechanical (E/M) impedance method for structural health monitoring and NDE. In: *Proceedings of the 5th annual international symposium on smart structures and materials*, vol.3329, San Diego, CA, 1–5 March 1998, pp. 536–547. New York: SPIE.
10. Naidu ASK, Bhalla S and Soh CK. Incipient damage localization with smart piezoelectric transducers using high-frequency actuation. *Proc SPIE* 2002; 4935: 473–484.
11. Lopes V Jr, Park G, Cudney HH, et al. Impedance-based structural health monitoring with artificial neural networks. *J Intel Mater Syst Struct* 2000; 11(3): 206–214.
12. Park G, Rutherford AG, Sohn H, et al. An outlier analysis framework for impedance-based structural health monitoring. *J Sound Vib* 2005; 286(1–2): 229–250.
13. Xu Q. Impact detection and location for a plate structure using least squares support vector machines. *Struct Health Monit* 2014; 13(1): 5–18.
14. Carden EP and Brownjohn JM. Arma modelled time-series classification for structural health monitoring of civil infrastructure. *Mech Syst Signal Pr* 2008; 22(2): 295–314.
15. Fan W and Qiao P. Vibration-based damage identification methods: a review and comparative study. *Struct Health Monit* 2011; 10(1): 83–111.
16. Gul M and Catbas FN. Damage assessment with ambient vibration data using a novel time series analysis methodology. *J Struct Eng* 2010; 137(12): 1518–1526.
17. Fassois SD, Sakaris CS and Sakellariou JS. Vibration-based damage localization and estimation via the stochastic functional model based method (FMBM): an overview. *Struct Health Monit* 2018; 17(6): 1335–1348.
18. Spanos NA, Sakellariou JS and Fassois SD. Vibration-response-only statistical time series structural health monitoring methods: a comprehensive assessment via a scale jacket structure. *Struct Health Monit*. Epub ahead of print 15 July 2019 Published online. <https://doi.org/10.1177/1475921719862487>
19. Fan X, Li J, Hao H, et al. Identification of minor structural damage based on electromechanical impedance sensitivity and sparse regularization. *J Aerospace Eng* 2018; 31(5): 04018061.
20. Kim J and Wang KW. An enhanced impedance-based damage identification method using adaptive piezoelectric circuitry. *Smart Mater Struct* 2014; 23(9): 095041.
21. Wang X and Tang J. Damage identification using piezoelectric impedance approach and spectral element method. *J Intel Mater Syst Struct* 2009; 20(8): 907–921.
22. Xia Y and Hao H. Statistical damage identification of structures with frequency changes. *J Sound Vib* 2003; 263(4): 853–870.
23. Cao P, Shuai Q and Tang J. Structural damage identification using piezoelectric impedance measurement with sparse inverse analysis. *Smart Mater Struct* 2018; 27(3): 035020.
24. Shuai Q, Zhou K, Zhou S, et al. Fault identification using piezoelectric impedance measurement and model-based intelligent inference with pre-screening. *Smart Mater Struct* 2017; 26(4): 045007.
25. Kennedy MC and O'Hagan A. Bayesian calibration of computer models. *J Royal Stat Soc: Series B* 2001; 63(3): 425–464.
26. Reese CS, Wilson AG, Hamada M, et al. Integrated analysis of computer and physical experiments. *Technometrics* 2004; 46(2): 153–164.
27. Vengazhiyil RJ and Melkote SN. Statistical adjustments to engineering models. *J Qual Technol* 2009; 41(4): 362–375.
28. Xiong Y, Chen W, Tsui K, et al. A better understanding of model updating strategies in validating engineering

- models. *Comput Method Appl Mech Eng* 2009; 198(15–16): 1327–1337.
29. Friswell M and Mottershead J. *Finite element model updating in structural dynamics*. Dordrecht: Springer, 2013.
 30. Doebbling SW, Farrar CR and Prime MB. A summary review of vibration-based damage identification methods. *Shock Vib Digest* 1998; 30(2): 91–105.
 31. Song M, Yousefianmoghdam S, Mohammadi ME, et al. An application of finite element model updating for damage assessment of a two-story reinforced concrete building and comparison with lidar. *Struct Health Monit* 2018; 17(5): 1129–1150.
 32. Behmanesh I and Moaveni B. Probabilistic identification of simulated damage on the Dowling hall footbridge through Bayesian finite element model updating. *Struct Control Health Monit* 2015; 22(3): 463–483.
 33. Rocchetta R, Broggi M, Huchet Q, et al. Online Bayesian model updating for structural health monitoring. *Mech Syst Signal Pr* 2018; 103: 174–195.
 34. Bayarri MJ, Berger JO, Paulo R, et al. A framework for validation of computer models. *Technometrics* 2007; 49(2): 138–154.
 35. Ezzat AA, Pourhabib A and Ding Y. Sequential design for functional calibration of computer models. *Technometrics* 2018; 60(3): 286–296.
 36. Pourhabib A, Huang JZ, Wang K, et al. Modulus prediction of buckypaper based on multi-fidelity analysis involving latent variables. *IIE Transactions* 2015; 47(2): 141–152.
 37. Li W, Chen S, Jiang Z, et al. Integrating Bayesian calibration, bias correction, and machine learning for the 2014 Sandia verification and validation challenge problem. *J Verif Valid Uncertain Quantif* 2016; 1(1): 011004.
 38. Simpson TW, Poplinski JD, Koch PN, et al. Metamodels for computer-based engineering design: survey and recommendations. *Eng Comput* 2001; 17(2): 129–150.
 39. Santner TJ, Williams BJ and Notz WI. *The design and analysis of computer experiments*. New York: Springer, 2003.
 40. Rasmussen CE and Williams CKI. *Gaussian processes for machine learning*. Cambridge, MA: MIT Press, 2006.
 41. Robert C and Casella G. *Monte Carlo statistical methods*. New York: Springer, 2013.
 42. Wang X and Tang J. Damage detection using piezoelectric admittance approach with inductive circuitry. *J Intel Mater Syst Struct* 2010; 21(7): 667–676.
 43. Zhou K, Shuai Q and Tang J. Adaptive damage detection using tunable piezoelectric admittance sensor and intelligent inference. In: *Proceedings of the ASME 2014 conference on smart materials, adaptive structures and intelligent systems SMASIS 2014*, Newport, Rhode Island, 8–10 September 2014.
 44. Kullaa J. Distinguishing between sensor fault, structural damage, and environmental or operational effects in structural health monitoring. *Mech Syst Signal Pr* 2011; 25(8): 2976–2989.
 45. Sohn H. Effects of environmental and operational variability on structural health monitoring. *Philos T R Soc A* 2006; 365(1851): 539–560.
 46. Arendt P, Apley D and Chen W. Quantification of model uncertainty: calibration, model discrepancy, and identifiability. *J Mech Design* 2012; 134(10): 100908.
 47. Tuo R and Wu CFJ. A theoretical framework for calibration in computer models: parametrization, estimation and convergence properties. *SIAM/ASA J Uncertain Quantif* 2016; 4(1): 767–795.
 48. Chen Z and Wang B. How priors of initial hyperparameters affect Gaussian process regression models. *Neurocomputing* 2018; 275: 1702–1710.